ADVANCED ENERGY MATERIALS
www.advenergymat.de

Spatially Confined MnO_2 Nanostructure Enabling Consecutive Reversible Charge Transfer from Mn(IV) to Mn(II) in a Mixed Pseudocapacitor-Battery Electrode

*Yu-Ting Weng, Hsiao-An Pan, Rung-Chuan Lee, Tzu-Yang Huang, Yun Chu, Jyh-Fu Lee, Hwo-Shuenn Sheu, and Nae-Lih Wu**

Mn oxides are highly important electrode materials for aqueous electrochemical energy storage devices, including batteries and supercapacitors. Although MnO_2 is a promising pseudocapacitor material because of its outstanding rate and capacity performance, its electrochemical instability in aqueous electrolyte prevents its use at low electrochemical potential. Here, the possibility of stabilizing MnO_2 electrode using SiO_2-confined nanostructure is demonstrated. Remarkably, an exceptionally good electrochemical stability under large negative polarization in aqueous (Li_2SO_4) electrolyte, usually unattainable for MnO_2-based electrode, is achieved. Even more interestingly, this MnO_2–SiO_2 nanostructured composite exhibits unique mixed pseudocapacitance-battery behaviors involving consecutive reversible charge transfer from Mn(IV) to Mn(II), which enable simultaneous high-capacity and high-rate characteristics, via different charge-transfer kinetic mechanisms. This suggests a strategy to design and stabilize electrochemical materials that are comprised of intrinsically unstable but high-performing component materials.

1. Introduction

Metal oxide pseudocapacitors,[1–7] which use fast redox reactions of electrochemically active metal oxide materials, are attractive energy-storage cells. The oxide pseudocapacitors can provide substantially higher power densities than rechargeable batteries, as well as substantially higher energy densities than electric double-layer capacitors.[8–12] Practical applications of the oxide pseudocapacitors, ranging from auxiliary power devices for batteries to stand-alone energy-storage devices, rely to a large extent on their energy-storage capacity. The specific energy (E) of a capacitor is described by

$$E = \frac{1}{2}C\Delta V^2 = \frac{1}{2}Q\Delta V \quad (1)$$

where C is the specific capacitance, ΔV is the operating voltage range, and Q is the specific charge-storage capacity. For improving the specific energy, both the charge-storage capacity and operating potential window (OPW) of the pseudocapacitor electrodes should be maximized.

First reported by Goodenough and coworkers,[13,14] MnO_2 has attracted substantial attention as a promising pseudocapacitor electrode material[15] because of its low cost, natural abundance, and environmental friendliness. The use of aqueous neutral electrolytes in MnO_2-based pseudocapacitors, in particular, provides superior device safety compared with those requiring either organic electrolytes or strong acidic (such as for RuO_2)[16] aqueous electrolytes.

Numerous studies have recently developed MnO_2 electrodes either in thin film[17–19] or as composites with various materials, such as graphene,[20,21] porous carbon foam,[22–24] and SiC,[25] to increase the solid–electrolyte contact area and tailor the electrode architectures for enhanced capacity and power performances.[17–25] However, until now, the charge-storage capacity of MnO_2-based pseudocapacitors has been limited to a small fraction of one-electron transfer between Mn(IV) and Mn(III) ions per unit formula of MnO_2 (e^-/MnO_2) with an OPW of ≤1 V.[26] Only in rare cases of either extremely low oxide loading[22,27,28] or mixed valences,[21] the MnO_2 electrodes have been reported to afford a specific charge capacity close to 1 e^-/MnO_2. To exceed this charge-storage limit, new strategies that enable reversible electron transfer between Mn ions of lower valences are required, and this also means that the OPW must be extended to lower potentials.

For an MnO_2 electrode in an aqueous electrolyte, the upper limit of its OPW is typically not related to the intrinsic properties of the oxide; however, it is limited by either water (solvent) or electrolyte anion (e.g., Cl^-) oxidation,[29] or current collector oxidation,[30] or the combination of both. For example, water oxidation causes oxygen bubbling, which may lead to active-layer loosening, and current collector oxidation causes an increase in the interfacial resistance between the active layer and the current collector.

By contrast, the lower limit of the OPW of an MnO_2 electrode is closely related to the fundamental electrochemical

Dr. Y.-T. Weng, H.-A. Pan, R.-C. Lee, T.-Y. Huang, Y. Chu, Prof. N.-L. Wu
Department of Chemical Engineering
National Taiwan University
Taipei 10617, Taiwan
E-mail: nlw001@ntu.edu.tw
Dr. J.-F. Lee, Dr. H.-S. Sheu
National Synchrotron Radiation Research Center
Hsinchu 30076, Taiwan

DOI: 10.1002/aenm.201500772

properties of the oxide. The most common cause to capacity fading occurring near the lower limit of the OPW is the dissolution of the oxide through soluble Mn(II) oxide formation. Mn(IV) is reduced to Mn(III) during cathodic discharging, and until below a certain potential, approximately 0 V (the potential is hereafter referenced to an Ag/AgCl/saturated KCl electrode; EG&G, 197 mV vs NHE at 25 °C), Mn(III) undergoes a disproportionation reaction to produce Mn(IV) and Mn(II), and Mn(II) is subsequently dissolved in the electrolyte:[27,28]

$$2\mathrm{Mn(III)OOH}_{(s)} \rightarrow \mathrm{Mn(IV)O}_{2(s)} + \mathrm{Mn}^{2+}_{(aq)} + 2\mathrm{OH}^{-}_{(aq)} \quad (2)$$

Mn^{2+} dissolution is confirmed by the formation of a brownish precipitate in the electrolyte. The precipitate originates from the reoxidation of the dissolved Mn^{2+} caused by O_2 in the electrolyte to form insoluble Mn oxides of high valences.

Further reduction of an MnO_2 electrode to well below 0 V has shown to result in an irreversible phase transformation to oxides of lower Mn valences.[31,32] These oxides typically have a more compact crystal structure and less favorable electrochemical activity than the starting MnO_2 phases,[31–33] which are mostly birnessite of different crystallinities. Birnessite consists of layers of edge-sharing $Mn(IV)O_6$ octahedra, providing two-dimensional (2D) tunnels with a large *d*-spacing (approximately 0.7 nm) between the *ab* planes. The tunnels facilitate the reversible intercalation of electrolyte cations occurring concurrently with electron transfer. The open lattice structure is considered crucial for achieving high charge-storage capacity.[26]

2. Results and Discussion

A new material design strategy was developed in the present study to extend the electrochemical stability of a MnO_2 electrode to negative polarization for enhancing the charge-storage capacity of the oxide electrode. This strategy was based on the concept of forming space-confined MnO_2 nanodomains of which the surfaces may be stabilized using an electrochemically inactive foreign oxide material that is capable of "retaining" Mn^{2+} ions through an interfacial bonding to avoid progressive erosion upon reduction.
Near 0 V,

$$2\mathrm{Mn(III)O(-O-M'-)}_{(s)} \rightarrow \mathrm{Mn(IV)O}_{2(s)} + \mathrm{Mn(II)(-O-M'-)}_{2(s)} \quad (3)$$

and well below 0 V,

$$\mathrm{Mn(III)O(-O-M'-)}_{(s)} \leftrightarrow \mathrm{Mn(II)(-O-M'-)}_{2} + e^{-} \quad (4)$$

where —O—M′— represents the stabilizing oxide. Furthermore, from the energetics point of view, a large surface-to-volume ratio plus an extensive interfacial interaction with the stabilizing oxide may cause different phase transformation behaviors of the MnO_2 nanodomains compared with those of a bulk MnO_2 aggregate, which is known to transform into phases of more compact lattice structures with decreasing charge-storage capacities.[31]

To select the surface oxide that is stable under a low potential in an aqueous environment, SiO_2 was used. Spherical mesoporous SiO_2 nanobeads were used as hosts within which MnO_2 was deposited. The deposition process was conducted through a hydrothermal process, which facilitates the formation of Mn—O—Si composite interfaces. As revealed in various geological settings,[34] the formation of Mn—Si oxides is facile under hydrothermal conditions. The precipitated oxide composite beads were finally treated with an alkaline solution to partially remove SiO_2 to produce a porous interior, which can increase the solid–electrolyte contact area. Detailed experimental procedures and conditions are described in the Experimental Section.

The resulting Mn–Si–O (MSO) composite was capable of undergoing consecutive reversible electron transfer from Mn(IV) to Mn(II) with an expanded OPW of up to 2 V in an aqueous electrolyte. Reversible charge transfer with a capacity substantially greater than one electron per Mn ion of a MnO_2 electrode in an aqueous electrolyte over thousands of cycles was demonstrated for the first time.

2.1. Material Characterization

The SiO_2 host particles exhibited granular surfaces (**Figure 1**a) and were mesoporous, containing regular arrays of pores (Figure 1b) with a narrow size distribution between 2.0 and 4.5 nm (Figure S1, Supporting Information) and a pore volume of 0.94 $cm^3\ g^{-1}$. However, the MSO composite particles resulting from the hydrothermal treatment exhibited solid smooth surfaces (Figure 1c) and appeared opaque under a transmission electron microscope (TEM) (Figure 1d). MnO_2 appeared to preferentially deposit within the SiO_2 particles; only a small amount of MnO_2 flakes was observed attached to the surfaces of the composite particles. In contrast to the black color of the control MnO_2 powder that was synthesized under the same conditions, except for the absence of SiO_2, the hydrothermally derived MSO composite powder exhibited a dark brownish color. After the treatment in an alkaline aqueous solution, the MSO particles turned porous and showed different hollow interior structures (Figure 1e–h), indicating partial dissolution of SiO_2. The SiO_2 could not be completely dissolved even with a prolonged etching treatment. Extensive energy-dispersive X-ray (EDX) line scan analysis indicated that the remaining skeletons of the hollow spheres after prolonged etching contained both Si and Mn (Figure 1e). In addition, Barrett–Joyner–Halenda (BJH) analysis (Figure S1, Supporting Information) indicated the absence of meso- and micropores in the etched MSO powder. Therefore, the etched MSO is a macroporous material with a solid skeleton. High-resolution TEM analysis revealed a domain structure within the remaining skeleton (Figure S2, Supporting Information). The Si oxide that remained in the skeleton exhibited chemical properties different from pure SiO_2, which would have dissolved in the alkaline solution. The brownish color of the MSO powder suggested doping of SiO_2 by Mn ions, and the doping may have reduced the solubility of SiO_2 in the alkaline solution. Composition analysis based on the inductively coupled plasma analysis was not successful because of incomplete leaching of Mn by the conventional nitric acid digestion treatment. Extensive EDX analysis indicated an average MnO_2 content of 32% (±3%) by weight.

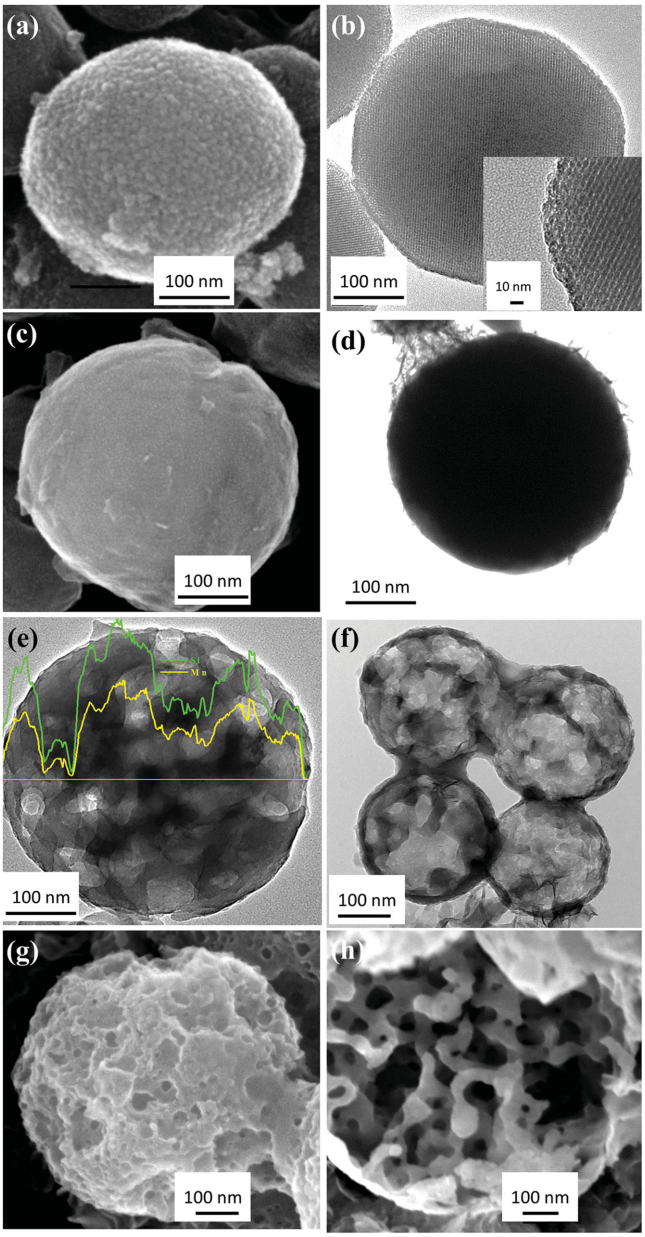

Figure 1. a) SEM and b) TEM images of mesoporous SiO_2 host particles; c) SEM and d) TEM images of hydrothermally derived fresh MSO composite particles; e,f) TEM and g,h) SEM images of MSO particles after dissolution in an aqueous alkaline solution. The solid lines in (e) delineate the EDX signal intensities of Si and Mn.

XRD analysis of the porous MSO composite showed reflections of MnO_2 birnessite along with a strong broad hump near $2\theta = \approx 22°$ (**Figure 2**). This hump can be attributed to the SiO_2 component. For comparison, the MnO_2 control powder showed reflections of only birnessite. The birnessite reflection peaks of the MSO sample were much broader than those of the MnO_2 control sample, suggesting that the average size of the birnessite crystallites in the MSO sample was substantially smaller than that in the control powder. Estimation of the crystallite size based on the Debye–Scherrer equation[35] gave an average birnessite crystallite size of 4.2 nm for the MSO powder and

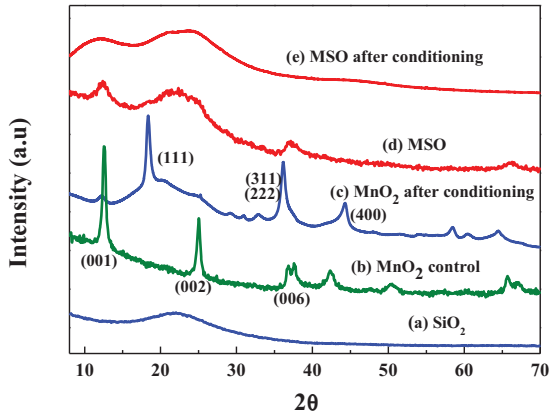

Figure 2. XRD patterns of (from bottom to top) a) the mesoporous SiO_2 host powder, b) MnO_2 control (birnessite), c) MnO_2 after the conditioning cycles (spinel) between –1 and 1 V, d) MSO composite powder, and e) MSO electrode after the conditioning cycles between –1 and 1 V.

13.8 nm for the MnO_2 control powder. The size of the birnessite crystallite in the MSO powder closely matched the pore dimensions of the starting SiO_2 powder. This dimensional consistency further proves that MnO_2 birnessite crystallites mainly form within the pores of the SiO_2 matrix.

All fresh electrodes were subjected to five conditioning cyclic voltammetry (CV) cycles over selected potential ranges prior to electrochemical characterization. For the MnO_2 control powder, the oxide particles within the electrode retained the birnessite structure after the conditioning cycles between 0 and 1 V, whereas they transformed into a crystalline spinel when the potential range was from –1 to 1 V (curve c, Figure 2). For the MSO electrode, the XRD birnessite reflections of the oxide particles disappeared after the conditioning cycles between –1 and 1 V; instead, only a small hump of birnessite (001) reflection, in addition to the hump of SiO_2, was detected using synchrotron XRD (curve e, Figure 2). The presence of the broad birnessite (001) hump indicates a highly defected layered structure of MnO_6 octahedra that retains the feature of a large *d*-spacing between the *ab* planes of birnessite; however, it lacks a long-range ordering along the *c*-axis. The XRD data acquired before and after the conditioning cycles indicate two major conclusions. First, electrochemical reduction of pure birnessite leads to an irreversible transformation into a more compact spinel structure. Second, the birnessite-to-spinel transformation is prohibited in the confined MnO_2 nanodomains within the MSO powder. The transformation from birnessite to spinel is accompanied by volume contraction. The extensive interfacial bonding between the MnO_2 nanodomains and SiO_2 might have prevented such contraction, thereby enabled the MSO electrode to retain a more open (although defected) birnessite structure suitable for a high charge-storage capacity.

Figure 3 shows the comparison of the Raman spectra of differently treated MnO_2-containing powders. As-synthesized MSO and MnO_2 control powders show two prominent Raman peaks at 556 and 621 cm^{-1}, respectively, and a small peak at 479 cm^{-1}, which can be attributed to the symmetric stretching vibrations of MnO_6 octahedra in the birnessite structure.[36] However, an additional small band at approximately 590 cm^{-1}

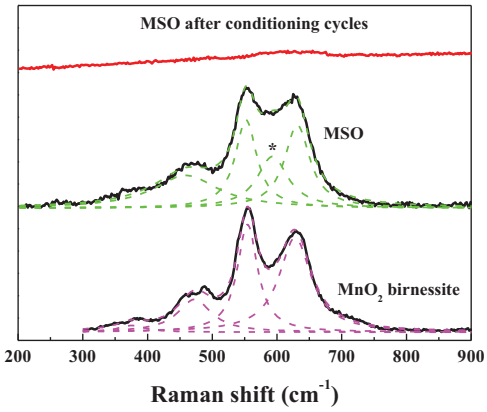

Figure 3. Raman spectra of the MnO_2 (birnessite) control powder, MSO composite powder, and MSO electrode after the conditioning cycles. The dashed lines delineate individual deconvoluted peaks and the fitted spectra.

is observed for the MSO powder (* in Figure 3), and this band, to our knowledge, cannot be attributed to any of the known Mn oxides of various valences. This new band is suggested to originate from the Mn—O—Si interfacial bonding. In addition, a new structural feature was observed in the extended X-ray absorption fine structure (EXAFS) analysis. As shown in **Figure 4**a, the EXAFS spectrum of the Mn *k*-edge of the MSO sample shows two prominent peaks at 1.28 and 2.44 Å, which respectively correspond to the typical Mn—O and Mn—Mn bond lengths within the layers of the MnO_6 octahedra of birnessite. An additional small peak was observed at 1.82 Å (* in Figure 4). This new peak corresponds to the bond length of a less polarized Mn—O bond than that in typical MnO_6 octahedra, and this is in accordance with the assumption of the Mn—O—Si bonding.[37]

After the conditioning cycles, the Raman band caused by MnO_6 was not observed for the MSO electrode (Figure 3). This result is in accordance with the XRD results, which indicate the loss of long-range ordering within the MnO_2 domains after the conditioning cycles (Figure 2). EXAFS Mn *k*-edge analysis of MSO after the conditioning cycles (Figure 4) showed a spectrum characteristic of birnessite, except for broadened Mn—O and Mn—Mn peaks, confirming that the Mn ions retained a local structure close to that of birnessite, but with increasing disordering.

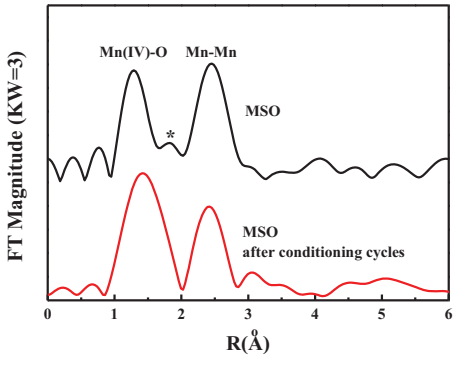

Figure 4. EXAFS spectra of the MSO powder and the MSO electrode after the conditioning cycles.

The material characterization data depict a unique nanostructure of the hydrothermally derived MSO powder, which contains birnessite nanodomains spatially confined by Mn-doped SiO_2 with an extensive Mn—O—Si interfacial bonding. After the conditioning cycles, the MnO_2 nanodomains in MSO turned amorphous and retained the feature of large 2D tunnels of the birnessite structure. The retention of the 2D tunnel structure is crucial because it can facilitate reversible cation intercalation involved in the charge–discharge process of the oxide electrode.

2.2. Electrochemical Characterization and Performance

The CV test of the MSO electrode showed a step reduction in the responsive current between the first and second conditioning cycles (Figure S3, Supporting Information). However, the voltammogram quickly converged to a stable profile within a few cycles. The step reduction in the charge-storage capacity within the initial conditioning cycles is in agreement with the aforementioned phase transformation of the MnO_2 nanodomains from crystalline birnessite to amorphous. Because of the transient behavior of the MSO electrode, all electrodes were subjected to five conditioning cycles prior to systematic electrochemical characterization. Therefore, all the following electrochemical data should be recognized as the properties of amorphous, but not crystalline, birnessite nanodomains.

Figure 5a,b shows respectively the plots of responsive current and dQ/dV (=current/scan-rate), which is equivalent to a capacitance, of the MSO electrode for CV measurements between −1 and 1 V. The MSO electrode exhibited a specific charge-storage capacity based on the mass of active material (AM; MnO_2 + SiO_2) of 572 C g^{-1}–AM at 2 mV s^{-1}. Because the SiO_2 component is inert, the MnO_2 nanodomains are estimated to have a specific capacity of 1786 C g^{-1}–MnO_2, which is equivalent to 1.61 e^-/MnO_2. The galvanostatic charge–discharge curves of the MSO electrodes exhibited a sloped potential profile with nearly 100% Coulombic efficiency (Figure 5c).

Figure 5b also shows the dQ/dV plot of the MSO electrode cycled at 2 mV s^{-1} between 0 and 1 V (the dashed line) for comparison. This plot has a nearly rectangular profile and is consistent with the pseudocapacitance that has previously been attributed to the surface redox reaction between the Mn(IV) and Mn(III) oxides, well known to the pure MnO_2 birnessite electrodes. From Figure 5b, it can be seen that the Mn(IV)–Mn(III) pseudocapacitance is the dominant charge-storage mechanism during the cathodic scan of the MSO electrode from 1 to 0 V at 2 mV s^{-1}.

Below 0 V during the cathodic scan at 2 mV s^{-1}, a wave peak occurs at −0.2 V, followed by a broad band up to −1 V. The charge transferred between 1 and −0.4 V approximately amounts to 1.0 e^-/MnO_2, and therefore it can be concluded that the wave peak at −0.2 V is mainly associated with bulk Mn(IV)-to-Mn(III) reduction. The broad band following the peak within the lower potential range can therefore be primarily ascribed to Mn(III)-to-Mn(II) reduction. The assignment of these two reduction events is consistent with that reported for the MnO_2 battery cathodes.[38] The anodic branch of the dQ/dV plot shows two prominent wave peaks at 0.17 and 0.92 V, respectively, and they correspond to the reverse of the aforementioned reduction

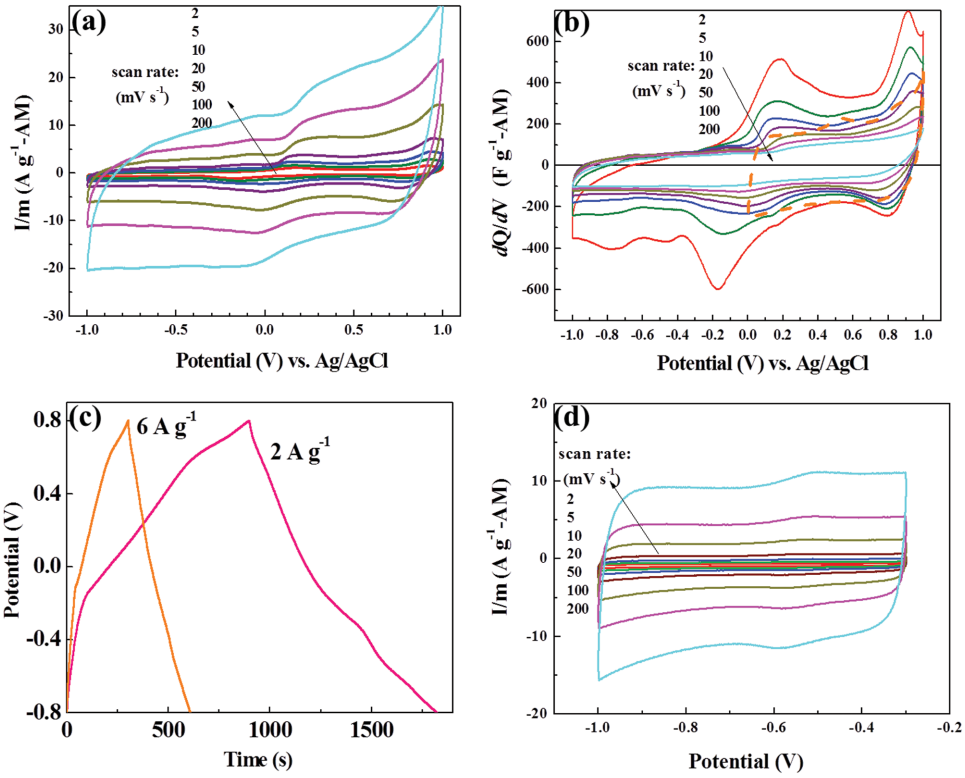

Figure 5. Electrochemical characterizations of the MSO electrode: a) current and b) dQ/dV plots of the MSO electrode by CV analysis at different scan rates between –1 and 1 V; the dashed line in (b) shows the dQ/dV plot acquired at 2 mV s^{-1} between 0 and 1 V; c) galvanostatic charge–discharge curves of the MSO electrode; d) current plots acquired between –1 and –0.3 V of the MSO electrode after being kept at –1 V for 24 h.

reactions. With an increase in the scan rate, the intensities of all the redox peaks in the dQ/dV plots of the MSO electrode progressively reduced (Figure 5b).

It is critical to understand if pseudocapacitance also arises from the Mn(III)–Mn(II) redox reactions. For the dQ/dV plot acquired at 2 mV s^{-1}, as shown in Figure 5b, the anodic curve showed negative capacitance after potential reversal at –1 V until it reached the onset of the peak of bulk Mn(II)-to-Mn(III) oxidation. The curve showed the characteristic expected from a battery electrode. However, when the scan rate was raised to 5 mV s^{-1} or higher scan rates, the anodic curves were found to turn positive shortly after the potential reversal at –1 V and then quickly attained nearly the same capacitance that extended over a substantial potential range up to ≈–0.3 V, where the bulk Mn(II)-to-Mn(III) oxidation peak started to emerge. The higher the scan rate, the earlier the constant-capacitance level was reached after the potential reversal. The constant-capacitance characteristic signifies the capacitor behavior, which is further verified in the following experiments.

To elucidate the pseudocapacitance behavior originating from the Mn(II)–Mn(III) redox reactions, an MSO electrode was first subjected to a cathodic scan from 1 to –1 V and then kept at –1 V for 24 h to enable completion of Mn(III)-to-Mn(II) reduction. The MSO electrode was subsequently subjected to CV scans between –1 and –0.3 V. By keeping the upper potential end below –0.3 V during the anodic scan, the contribution of the bulk Mn(II)–Mn(III) redox reactions to the responsive current was minimized, if not completely avoided. As shown in Figure 5d, nearly rectangular current plots typical of a capacitor were indeed obtained. The correlation of the responsive current with the scan rate gave an average specific capacitance of 51 (± 3) F g^{-1}–AM, which was close to the constant capacitance read from the anodic curves within the potential range between –0.6 and –0.3 V in Figure 5b. Given the small surface area of the MSO powder as shown by the adsorption data (Figure S1, Supporting Information), the capacitance is too high to be accounted for by the electric double-layer capacitance and is therefore pseudocapacitance in origin.

Figure 6 schematically summarizes the aforementioned charge-storage mechanisms based on the combination of the dQ/dV plots of 2 and 100 mV s^{-1}. The pseudocapacitance originating from the Mn(IV)–Mn(III) charge transfer, denoted as PC (IV)–(III), occurs between 0 and 1 V, and the specific capacitance is 181 F g^{-1}–AM at the scan rate of 2 mV s^{-1}. Pseudocapacitance from Mn(III)–Mn(II) redox reactions, denoted as PC (III)–(II), commences at certain potential below 0 V. The transition between PC (IV)–(III) and PC (III)–(II) is partially delineated by the anodic curve of the dQ/dV plot of 100 mV s^{-1}. By taking the constant capacitance of 51 F g^{-1} for PC (III)–(II), the overall charge-storage capacity of pseudocapacitance over the entire 2 V range is estimated to be 0.65 e^{-}/MnO_2, which accounts for nearly 40% of the total charge-storage capacity, at the scan rate of 2 mV s^{-1}. Battery behavior involving bulk reduction from Mn(IV) to Mn(III) and then to Mn(II), denoted respectively as B (IV)→(III) and B (III)→(II) in Figure 6, takes place primarily between 0 and –1 V. On the other hand, the

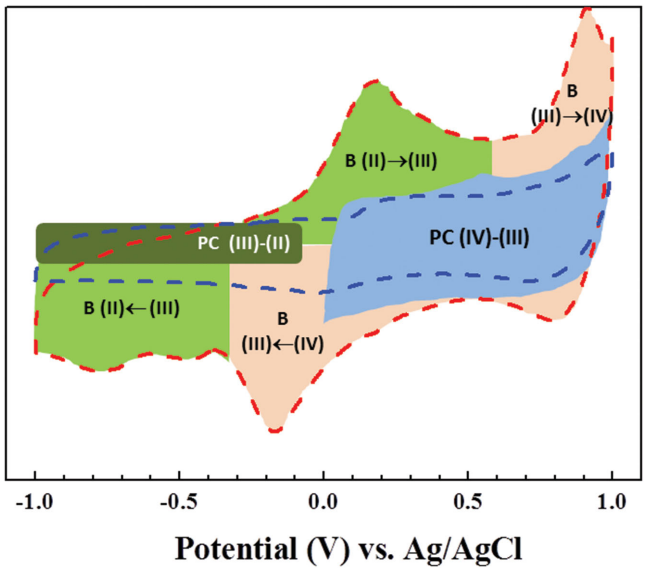

Figure 6. Schematic expression of various charge-storage mechanisms as a function of potential; B: battery behavior; PC: pseudocapacitance; (IV), (III), and (II): Mn ions having valences of 4, 3, and 2, respectively. The red and blue lines are the dQ/dV plots of the MSO electrode acquired at 2 and 100 mV s^{-1}, respectively.

battery behavior involving oxidation from Mn(II) to Mn(III) and then to Mn(IV), i.e., B (II)→(III) and B(III)→(IV), occur concurrently with PC (IV)–(III) during the anodic scan from –0.3 to 1 V. Overlapping over certain potential ranges between the consecutive reduction or oxidation reactions are expected. Figure 6 also illustrates the fact that the battery behavior provides a substantial amount of charge-storage capacity additional to pseudocapacitance at low scan rates.

For the MnO_2 control electrode, by contrast, the two redox pairs could not be clearly identified but showed broad humps in the dQ/dV plots of **Figure 7** even at the scan rate of 2 mV s^{-1}. The poorly resolved redox peaks indicate that the charge-transfer kinetics taking place in the MnO_2 control electrode is much slower than that in the MSO electrode. Moreover, the anodic curves of the dQ/dV plots always showed negative capacitances below –0.4 V, irrespective of the scan rate, indicating the lack

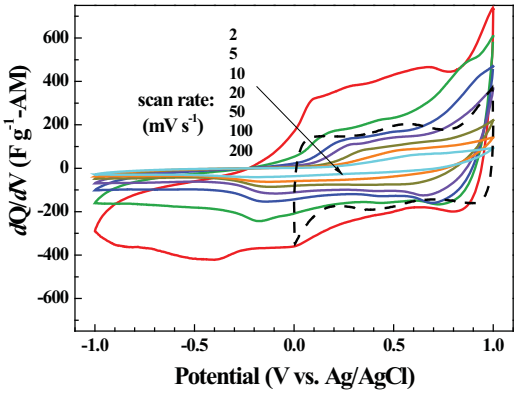

Figure 7. dQ/dV plots of the MnO_2 control electrode acquired between –1 and 1 V (dashed line: dQ/dV plot at 2 mV s^{-1} between 0 and 1 V).

of pseudocapacitance from Mn(III)–Mn(II) redox reactions. Figure 7 also plots the dQ/dV plot of the MnO_2 control electrode measured between 0 and 1 V (177 F g^{-1}–MnO_2). It is interesting to note that, while the MnO_2 control electrode and the MSO electrode behaves similarly when scanned between 1 and 0 V (dashed lines in Figures 5b and 7), they perform dramatically differently when the lower end of the OPW is extended to –1 V.

Figure 8a,b plots the specific capacity data based on either MnO_2 (C g^{-1}–MnO_2) or total AM loading (C g^{-1}–AM) versus scan rate. The MSO electrode possesses a specific capacity of 1786 C g^{-1}–MnO_2 (Figure 8a) or 572 C g^{-1}–AM (Figure 8b) at the scan rate of 2 mV s^{-1}. They are markedly higher than that (363 C g^{-1}–MnO_2) of the MnO_2 control electrode, and the difference increases with increasing scan rate. The AM specific capacity of the MSO electrode at a scan rate of 200 mV s^{-1}, for example, is 157 C g^{-1}–AM, which is more than five times that (30 C g^{-1}–AM) of the MnO_2 control electrode. Furthermore, capacity data calculated from recent literature on various MnO_2-based composite pseudocapacitive electrodes, such as MnO_2–metal,[17,18] MnO_2–C[21,22] and MnO_2–SiC,[25] have also been plotted in Figure 8a,b for comparison. (The literature data reported on the basis of MnO_2 are plotted in Figure 8a, while those on total AM loading in Figure 8b.) As shown, compared with these electrodes, the MSO electrode shows superior or comparable charge-storage capacities and rate performance. It is worth mentioning that the MSO electrode is operable over a potential range of 2 V (–1 to 1 V; Figure 5a,b), whereas those reported in the literature are practically no greater than 1 V. Therefore, according to Equation (1), the MSO electrode may afford an even greater advantage in terms of the energy-storage capacity in the full-cell configuration.

The cycling stability of the MSO electrode was tested using CV scanning at 20 mV s^{-1}, and the electrode retained 68% stability after 5000 cycles (**Figure 9**). By contrast, the MnO_2 control electrode lost more than 90% capacity in <500 cycles. The cycle test of the MnO_2 control electrode led to the formation of a brownish precipitate in the electrolyte, indicating extensive Mn^{2+} dissolution (inset in Figure 9). By contrast, no precipitation was observed during the cycle test of the MSO electrode, indicating no Mn^{2+} dissolution. These results clearly show that the MSO material design successively protects MnO_2 from erosion when the electrode operates in a low-potential region.

2.3. Charge-Transfer Kinetic Mechanisms

Electron transfer during the charge–discharge of MnO_2 pseudocapacitive electrodes has been shown to involve not only the adsorption–desorption of cations, such as electrolyte cation (Li^+ in this case) and proton, at surfaces but also the insertion–extraction of the cations through the crystallographic tunnels of various dimensions and sizes within the crystal structures of MnO_2 polymorphs.[39–40] The cation insertion–extraction may proceed through two types of kinetic mechanisms, namely the homogeneous solid–solution intercalation (SSI) mechanism and the heterogeneous two-phase reaction (TPR) mechanism. In the SSI mechanism, the inserting cations randomly and homogenously enter/leave the host matrix without creating

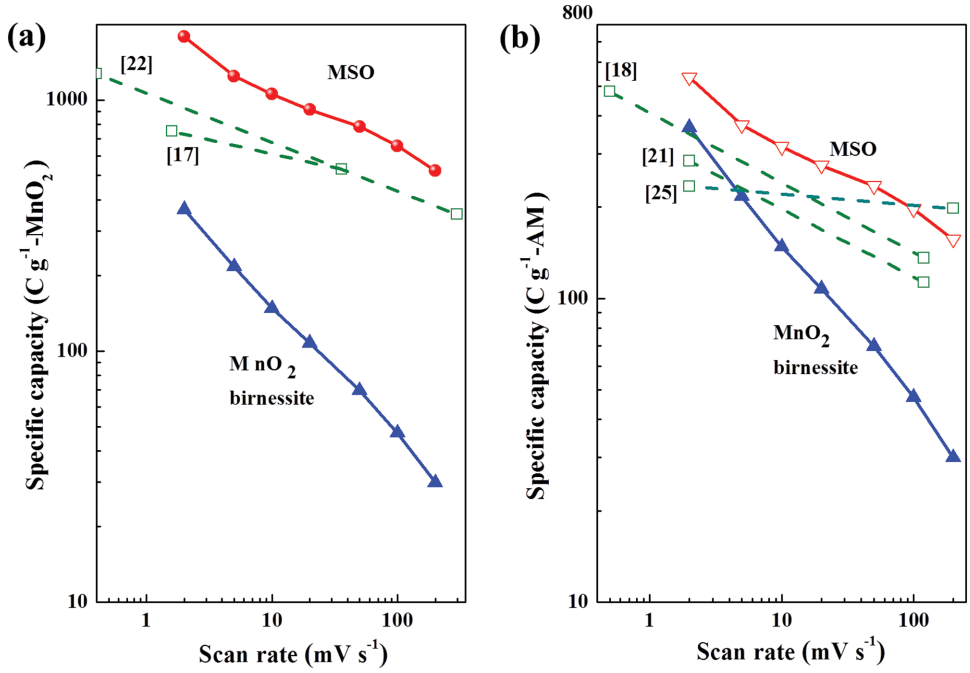

Figure 8. Specific capacity versus scan rate for MSO and MnO_2 control electrodes; a) specific capacity based on MnO_2 only; b) specific capacity based on total mass of active material (AM; composite). The open-square points are data derived from the literature and they are calculated based on reported specific capacitance values and operating potential windows.

a new domain therein. By contrast, in the TPR mechanism, domains having different, either local or long-ranged, structures coexist within the AM during charge–discharge. The TPR mechanism involves nucleation and growth of the evolving domains, whereas the SSI mechanism does not.

The kinetic mechanism of the MSO electrode was investigated based on in operando X-ray absorption near-edge spectroscopy (XANES) analysis of the Mn *k*-edge absorption. The nature of the Mn ions within the bulk of the MnO_2 nanodomains may be probed based on the Mn *k*-edge energy and the profile of the near-edge absorption spectrum. As indicated by the absorption spectra of standard Mn oxides shown in **Figure 10**a, the Mn *k*-edge energy in general decreases with reducing Mn valence,[25,34,35] and some of the Mn oxides, for instance Mn_3O_4 and MnO, exhibit unique spectrum profiles that are distinctly different from those of the other Mn oxides.

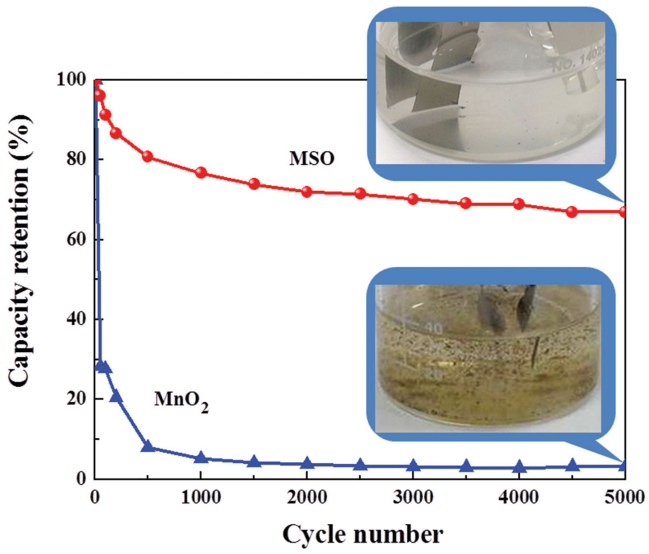

Figure 9. Specific capacity versus the cycle number for MSO and MnO_2 electrodes. The insets show the solution at the end of the cycling tests.

During the cathodic CV scan from 1 to −1 V, as shown in Figure 10b, the absorption edge progressively shifted toward lower energies. The Mn *k*-edge of the oxide nanodomains coincided with that of Mn_3O_4 at −1 V, which corresponds to a Mn valence of 2.7. The overall change in Mn valence for the cathodic scan from 1 to −1 V determined from XANES was approximately 1.3, which was slightly smaller than that (1.6) from the CV measurement. However, it should be pointed out that the structure of the MnO_2 nanodomains is not the same as the standard samples of the Mn oxides, and therefore the XANES analysis gives only approximated values of Mn valence.

It is also found in Figure 10b that there is no isosbestic point existing among all the absorption spectra falling within the range between Mn(IV) and Mn(III). The data indicate that the Mn oxide domains remained single-phased and the charge transfer between Mn(IV) and Mn(III) proceeds through the SSI mechanism (**Figure 11**a).

During the anodic scan from −1 to −0.3 V, the absorption edge further shifted to lower energies (Figure 10c); that is, while the entire electrode was undergoing oxidation, the average valence of the Mn ions within the bulk Mn oxide domains continued to decrease. The data indicate that charge transfer from Mn(III) to Mn(II) is incomplete when the cathodic scan reaches −1 V and that a battery current continues to flow into the electrode during the early stage of the anodic scan, as indicated by a negative capacitance appearing during the early stage of the

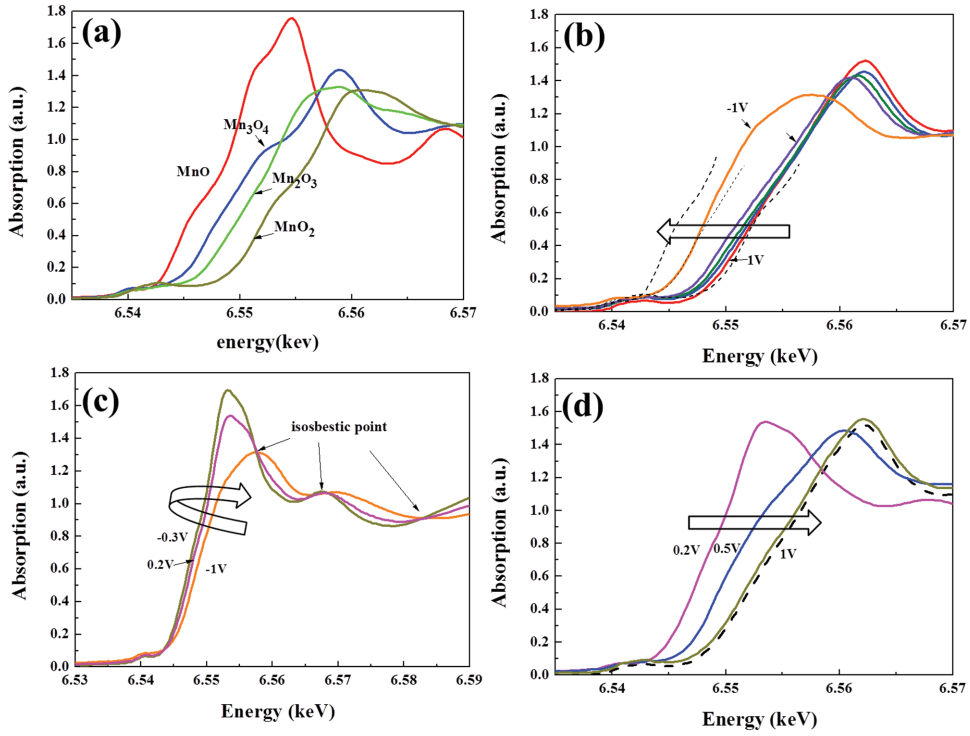

Figure 10. Mn *k*-edge XANES analysis: a) spectra of standard powders; b) in operando spectra of the MSO electrode acquired during reduction from 1 to –1 V (the dashed lines delineate the edge profiles of standard powders including, from left to right, MnO, Mn_3O_4, and MnO_2); c) spectra during oxidation from –1 to 0.2 V; and d) spectra during oxidation from 0.2 to 1 V (the dashed line indicates the starting spectrum of the electrode).

anodic scan at the scan rate of 2 mV s^{-1} (Figure 5b). Isosbestic points are observed among the absorption spectra, including those taken at –1, –0.3, and 0.2 V (Figure 10c), within the range of Mn(II) and Mn(III), indicating that the cation insertion/extraction proceeds through the TPR mechanism (Figure 11b).

With further oxidation from 0.5 to 1 V, the absorption spectrum progressively shifted back to its position at the beginning of the cycle, indicating high reversibility of the entire charge transfer process (Figure 10d).

Figure 12 shows the comparison of the EXAFS spectra acquired within the potential ranges of the two charge-transfer mechanisms. The spectra acquired at 1 and –0.5 V, which fall within the SSI range, show the same two prominent peaks that are characteristic of Mn(IV)–O and Mn(IV)–Mn(IV) of birnessite. The spectra indicate that the fundamental birnessite structures do not change within this range, and this is consistent with the SSI mechanism. A decrease in intensity with an increase in Li ion upon reduction is due to the scattering caused by the inserting Li ions, and it is commonly observed

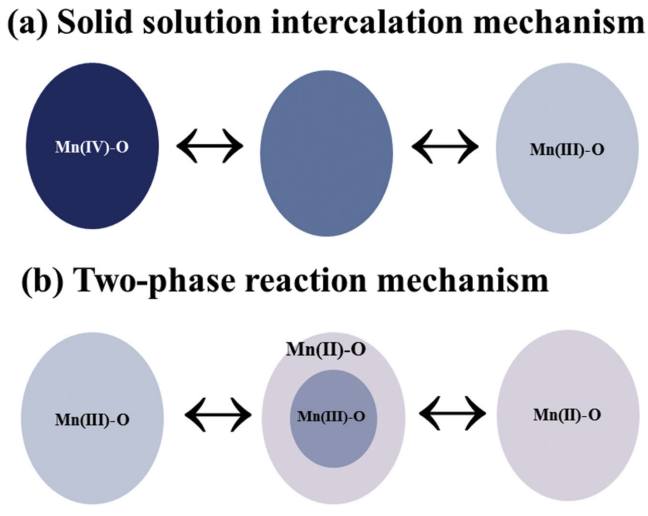

Figure 11. Schematics of the charge-transfer mechanisms involved in the MSO electrode; a) the solid–solution intercalation mechanism for charge transfer between Mn(IV)O and Mn(III)O and b) the two-phase reaction mechanism between Mn(III)O and Mn(II)O.

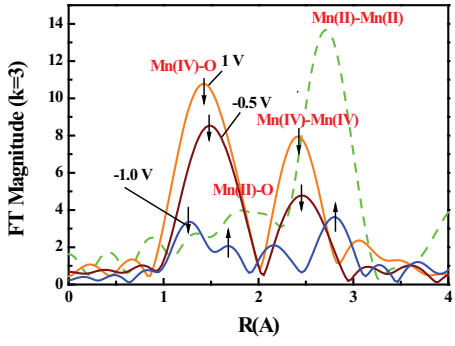

Figure 12. EXAFS spectra of the MSO electrode acquired at three potentials, namely 1, –0.5, and –1 V, during a complete CV cycle between 1 and –1 V. The dashed line plots the spectrum of MnO standard sample. The down arrows locate the major peaks of the Mn(IV)–O phase, while the up arrows locate those of the Mn(II)–O phase.

during the lithiation of an Li battery electrode.[41] By contrast, the spectrum acquired at –1 V, which is within the TPR range, shows two sets of Mn—O and Mn—Mn peaks, including one set of birnessite (the Mn—Mn peak is too weak to be observed) and the other set close to that of crystalline MnO. The coexistence of domains of Mn oxides with different local structures is consistent with the TPR mechanism.

Finally, the XANES spectra of the MnO_2 control electrode acquired at different potentials (Figure S4, Supporting Information) showed profile characteristics of Mn(IV) with an edge front shifting over a substantially narrower energy range than that observed for the MSO electrode. The profile was irreversible, showing a reduction in the edge energy upon the completion of a CV cycle.

3. Conclusion

A novel material design strategy is demonstrated to substantially widen (up to 2 V) the OPW of MnO_2-based aqueous pseudocapacitive electrode and to enable consecutive reversible charge transfer from Mn(IV) to Mn(II) over thousands of cycles. The material design involves forming spatially confined MnO_2 nanodomains of which the surfaces are surrounded by electrochemically inactive SiO_2 with extensive interfacial Mn—O—Si bonding. The resulting MSO electrode exhibits mixed pseudocapacitor–battery behavior with high charge-storage capacity in an aqueous Li_2SO_4 electrolyte between –1 and 1 V with no Mn ion dissolution, which otherwise occurs in the conventional bulk MnO_2 electrode and leads to fast charge-storage capacity deterioration, during cycling. In operando synchrotron X-ray absorption analyses reveal a two-step charge-transfer process, consisting of a solid–solution mechanism between Mn(IV) and Mn(III) and a TPR mechanism between Mn(III) and Mn(II). The presented MSO nanostructure holds great promise for high-capacity, high-energy supercapacitor applications.

4. Experimental Section

Synthesis of MnO_2/SiO_2 Nanostructured Composite Material: Mesoporous SiO_2 nanoparticles were purchased from Sigma Aldrich and all chemical reagents used in this study were of an analytical grade. To synthesize MnO_2, 0.5 g of $KMnO_4$ was added to 40 mL of aqueous dispersion solution containing 1.92 g of SiO_2, and the solution was treated at 150 °C for 48 h. After washing with distilled water, brownish MnO_2/SiO_2 powder (precipitate) was obtained. The product was subsequently etched using 1 M NaOH solution for 12 h, washed with distilled water, and finally dried in air at 60 °C.

Material Characterization: Microstructural characterization was conducted using scanning electron microscopy (SEM; JSM-7600F, JEOL) and a TEM (FEI Tecnai TF20, Philips). Pore-size distribution of powder samples were determined using BJH analysis on N_2 adsorption with Micromeritics, ASAP2020. Raman scattering spectra were obtained using a PROMaker system mounted with one thermoelectrically cooled CCD of 1024 × 256 pixels. Powder XRD was performed using a diffractometer (X-pert/Philips) with Cu K_α radiation. Synchrotron XRD and XANES analyses were conducted using the beam-line 01-C2 (for XRD) and 17-C1 (for XANES) facilities at the National Synchrotron Radiation Research Center in Taiwan. In operando XANES analysis was performed using Ti mesh as the current collector and by placing the electrode in an acrylic cell. The two sides of the cell were perforated and sealed using Kapton foils to allow the probing beam to pass through the cell. The scan rate for the in operando XANES analyses was 2 mV s^{-1}, and the scan was stopped at each selected potential for 10 min before collecting data.

Electrochemical Characterization: To prepare the working electrode, an electroactive material, carbon black (Aldrich), multi-wall carbon nanotube (Scientech Corporation), and polytetrafluoroethylene (Aldrich) with weight ratios of 70/10/5/15 in dry basis were mixed with ethanol to produce a slurry, which was then casted into a film on a Ti foil and dried at 50 °C for 60 min. The electrochemical properties of the electrodes were characterized using CV and galvanostatic charge–discharge on a potentiostat (608, CH Instruments; Eco Chemie PGSTAT30, AUTOLAB) in 2 M Li_2SO_4 aqueous solution. The fundamental electrochemical properties of the electrodes were characterized in a three-electrode configuration, which consists of a working electrode, platinum foil counter electrode, and Ag/AgCl/saturated KCl (EG&G, 197 mV vs NHE at 25 °C) reference electrode. The specific capacity (Q_s) was calculated by integrating the current over an entire CV cycle:

$$Q_s = \left(\oint I dV\right) \Big/ (\upsilon \times m \times 2), \tag{5}$$

where I is the current, v is the potential scan rate, and m is the mass of either MnO_2 or total AM.

Supporting Information

Supporting Information is available from the Wiley Online Library or from the author.

Acknowledgements

The authors acknowledge Prof. Patrice Simon, Dr. Pierre-Louis Taberna, and Wan-Yu Tsai at Université Paul Sabatier for insightful discussions. This work was financially supported by the Ministry of Science and Technology (MOST), Taiwan (NSC 101–2221-E-002–160-MY3; NSC 102–3113-P-006–012). One of the authors, Y.-T.W. would like to thank MOST postdoctor fellowship (MOST 103–2811-E-002–003, 104–2811-E-002–005).

Received: April 19, 2015
Revised: June 10, 2015
Published online:

[1] J. Ji, L. L. Zhang, H. Ji, Y. Li, X. Zhao, X. Bai, X. Fan, F. Zhang, R. S. Ruoff, *ACS Nano* **2013**, *7*, 6237.
[2] G. Wang, L. Zhang, J. Zhang, *Chem. Soc. Rev.* **2012**, *41*, 797.
[3] X. Lu, G. Wang, T. Zhai, M. Yu, J. Gan, Y. Tong, Y. Li, *Nano Lett.* **2012**, *12*, 1690.
[4] W. Wei, X. Cui, W. Chen, D. G. Ivey, *Chem. Soc. Rev.* **2011**, *40*, 1697.
[5] X. Lang, A. Hirata, T. Fujita, M. Chen, *Nat. Nanotechnol.* **2011**, *6*, 232.
[6] Z. S. Wu, D. W. Wang, W. Ren, J. Zhao, G. Zhou, F. Li, H. M. Cheng, *Adv. Funct. Mater.* **2010**, *20*, 3595.
[7] P. Simon, Y. Gogotsi, *Nat. Mater.* **2008**, *7*, 845.
[8] L. L. Zhang, X. S. Zhao, *Chem. Soc. Rev.* **2009**, *38*, 2520.
[9] C. Liu, Z. Yu, D. Neff, A. Zhamu, B. Z. Jang, *Nano Lett.* **2010**, *10*, 4863.
[10] Y. Zhu, S. Murali, M. D. Stoller, K. J. Ganesh, W. Cai, P. J. Ferreira, A. Pirkle, R. M. Wallace, K. A. Cychosz, M. Thommes, D. Su, E. A. Stach, R. S. Ruoff, *Science.* **2011**, *332*, 1537.
[11] B. Xu, S. Yue, Z. Sui, X. Zhang, S. Hou, G. Cao, Y. Yang, *Energy Environ. Sci.* **2011**, *4*, 2826.

[12] B. G. Choi, M. H. Yang, W. H. Hong, J. W. Choi, Y. S. Huh, *ACS Nano* **2012**, *6*, 4020.
[13] H. Y. Lee, J. B. Goodenough, *J. Solid State Chem.* **1999**, *144*, 220.
[14] H. Y. Lee, V. Manivannan, J. B. Goodenough, *C. R. Acad. Sci., Ser. IIC: Chim.* **1999**, *2*, 565.
[15] W. Wei, X. Cui, W. Chen, D. G. Ivey, *Chem. Soc. Rev.* **2011**, *40*, 1697.
[16] J. P. Zheng, P. J. Cygan, T. R. Jow, *J. Electrochem. Soc.* **1995**, *142*, 2699.
[17] Q. Li, Z. L. Wang, G. R. Li, R. Guo, L. X. Ding, Y. X. Tong, *Nano Lett.* **2012**, *12*, 3803.
[18] X. Lang, A. Hirata, T. Fujita, M. Chen, *Nat. Nanotechnol.* **2011**, *6*, 232.
[19] M. K. Song, S. Cheng, H. Chen, W. Qin, K. W. Nam, S. Xu, X. Q. Yang, A. Bongiorno, J. Lee, J. Bai, T. A. Tyson, J. Cho, M. Liu, *Nano Lett.* **2012**, *12*, 3483.
[20] S. He, W. Chen, *Nanoscale* **2015**, *7*, 6957.
[21] G. Yu, L. Hu, M. Vosgueritchian, H. Wang, X. Xie, J. R. McDonough, X. Cui, Y. Cui, Z. Bao, *Nano Lett.* **2011**, *11*, 2905.
[22] S. He, W. Chen, *J. Power Sources* **2014**, *262*, 391.
[23] M. Liu, L. Gan, W. Xiong, Z. Xu, D. Zhu, L. Chen, *J. Mater. Chem. A* **2014**, *2*, 2555.
[24] S. He, C. Hu, H. Hou, W. Chen, *J. Power Sources* **2014**, *246*, 754.
[25] M. Kim, J. Kim, *ACS Appl. Mater. Interfaces* **2014**, *6*, 9036.
[26] O. Ghodbane, J. L. Pascal, F. Favier, *ACS Appl. Mater. Interfaces* **2009**, *1*, 1130.
[27] S. C. Pang, M. A. Anderson, T. W. Chapman, *J. Electrochem. Soc.* **2000**, *147*, 444.
[28] S. C. Pang, M. A. Anderson, *J. Mater. Res.* **2000**, *15*, 2096.
[29] T. Brousse, M. Toupin, D. Bélanger, *J. Electrochem. Soc.* **2004**, *151*, A614.
[30] F. Ataherian, N. L. Wu, *J. Electrochem. Soc.* **2011**, *158*, A422.
[31] K. W. Nam, M. G. Kim, K. B. Kim, *J. Phys. Chem. C* **2007**, *111*, 749.
[32] F. Ataherian, K. T. Lee, N. L. Wu, *Electrochim. Acta* **2010**, *55*, 7429.
[33] Y. Dai, K. Wang, J. Xie, *Appl. Phys. Lett.* **2007**, *90*, 104102.
[34] Z. Sun, H. Zhou, G. P. Glasby, Q. Yang, X. Yin, J. Li, Z. Chen, *J. Asian Earth Sci.* **2012**, *43*, 64.
[35] F. W. Jones, *Proc. R. Soc., Ser. A* **1938**, *166*, 16.
[36] C. Julien, M. Massot, R. Baddour-Hadjean, S. Franger, S. Bach, J. P. Pereira-Ramos, *Solid State Ionics* **2003**, *159*, 345.
[37] G. V. Gibbs, R. T. Downs, D. F. Cox, K. M. Rosso, N. L. Ross, A. Kirfel, T. Lippmann, W. Morgenroth, T. D. Crawford, *J. Phys. Chem. A* **2008**, *112*, 8811.
[38] D. Y. Qu, B. E. Conway, L. Bai, Y. H. Zhou, W. A. Adams, *J. Appl. Electrochem.* **1993**, *23*, 693.
[39] S. L. Kuo, N. L. Wu, *J. Electrochem. Soc.* **2006**, *153*, A1317.
[40] O. Ghodbane, F. Ataherian, N. L. Wu, F. Favier, *J. Power Sources* **2012**, *206*, 454.
[41] H. Liu, F. C. Strobridge, O. J. Borkiewicz, K. M. Wiaderek, K. W. Chapman, P. J. Chupas, C. P. Grey, *Science* **2014**, *344*, 1252817.